Journal of
Micro/Nanolithography,
MEMS, and MOEMS

Nanolithography.SPIEDigitalLibrary.org

Measurement of the phase defect size using a scanning probe microscope and at-wavelength inspection tool

Tsuyoshi Amano
Tsukasa Abe

SPIE.

Measurement of the phase defect size using a scanning probe microscope and at-wavelength inspection tool

Tsuyoshi Amano[a,*] **and Tsukasa Abe**[b]
[a]EUVL Infrastructure Development Center, Inc., Onogawa, Tsukuba, Ibaraki 305-8569, Japan
[b]Dai Nippon Printing Co., Ltd., Fukuoka, Fujimino, Saitama 356-8507, Japan

Abstract. Predicting the lithography impact of a phase defect embedded in a mask used for extreme ultraviolet lithography on the printed image on wafer is a challenging task. In this study, two types of measurement tools were employed to characterize the phase defects. The prior measurement tool was a scanning probe microscope used for measuring the surface topography of phase defects, and the second was an at-wavelength dark-field inspection tool capable of capturing a phase defect and then calculating the defect detection signal intensity (DSI) from those images. A programmed phase defect mask with various lateral sizes and depths was prepared. The sizes and DSIs were then measured. The measured data indicated that the DSIs did not directly correlate with the phase defect volumes. The influence of the phase defects on the printed image on a wafer was also calculated using a lithography simulator. The simulation results indicated that the printed critical dimensions (CDs) were strongly correlated with the DSIs rather than with the phase defect volumes. As a result, the influence of the phase defect on the printed CD can be predicted from the values of the DSIs. [DOI: 10.1117/1.JMM.14.3.033508]

Keywords: extreme ultraviolet; phase defect; inspection; defect mitigation.

Paper 15020P received Mar. 15, 2015; accepted for publication Aug. 4, 2015; published online Aug. 21, 2015.

1 Introduction

Extreme ultraviolet lithography (EUVL) is considered the most promising next-generation lithography after the point at which 193-nm immersion lithography will not be able to deliver smaller features. However, the path to establish the EUVL is not without technical difficulties. For example, a lack of sufficient light-source power, particle-free mask handling, defect-free and flat mask blanks,[1–5] and resist material development[6,7] all need to be addressed. From the viewpoint of EUV mask fabrication, mask pattern defect inspection[8–11] and repair[12–14] are some of the most demanding tasks to be dealt with. The reason is that for EUVL generation, the device pattern feature size happens to be exceedingly small and calls for a higher repairing accuracy than would be required in optical lithography.[15–17] Regarding the types of the defects, the nature of the pattern defects in the EUV mask is mostly the same as in the case of optical masks except for those defects that are classified as reflective multilayer defects, such as bump or pit phase defects. These propagate through the multilayer mirror during its deposition on to the substrate surface and are hard to repair.[18] Therefore, to reduce the effect of a phase defect on the printed image, two elimination methods are suggested. One method is to cover the phase defects beneath an absorber pattern by shifting the position of the device pattern during mask patterning.[19–21] The other is to eliminate the influence of the phase error by removing the absorber at the close proximity of the phase defects after fabricating the device pattern.[22] In order to make these methods successful, it is necessary to measure the size or volume of the phase defects. This can be done using a scanning probe microscope (SPM). Additionally, an at-wavelength defect inspection tool has been found to be helpful.[23–25] The at-wavelength defect inspection tool has considerable advantages over other defect inspection tools using deep ultraviolet light optics. Employing the EUV light has the main advantage of excellent capability of detecting phase defects, but also predicts the lithographic impact of the detected phase defect on a wafer better.[26–30]

*Address all correspondence to: Tsuyoshi Amano, E-mail: tsuyoshi.amano@eidec.co.jp

2 Experiment

2.1 *Preparation of a Programmed Phase Defect Extreme Ultraviolet Mask*

A programmed pit phase defect EUV blank was prepared. The EUV mask used in this study consisted of a reflective multilayer deposited on a quartz substrate. The multilayer consisted of 40-bilayer Mo (2.2-nm thick)/Si (4.8-nm thick) with Ru (2.5-nm thick) as a capping layer. For this purpose, seeds for phase defects on a quartz substrate were fabricated through resist patterning and quartz etching processes before coating the multilayer. The quartz substrate was coated with a chrome layer as a hard mask in order to obtain enough etching selectivity against the quartz. A photoresist layer was coated on the chrome layer and a set of seeds to serve as phase defects, and guide patterns were drawn on the photoresist layer by an electron-beam pattern writing tool (JBX-9300FS, JEOL Ltd, Tokyo, Japan). After developing the photoresist layer, the chrome layer was etched. Then the quartz substrate was etched followed by photoresist stripping. To obtain different depths of the phase defects, resist patterning and quartz etching processes were carried out three times under different quartz etching process conditions. Figure 1 shows the design of the programmed phase

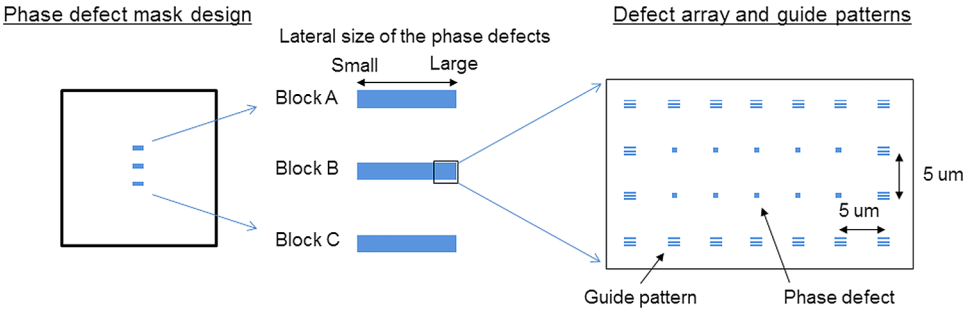

Fig. 1 Design of the programmed phase defect mask and an arrangement of the programmed phase defects.

defect mask. Blocks A, B, and C indicate the same design of the phase defects but have different etch depths as mentioned earlier. The lateral sizes of the phase defects were 30, 40, 50, 60, 70, 80, and 100 nm in diameter. The phase defects were arrayed in 5×2 matrices with their pitch values of 5 μm surrounded by guide patterns of 100-nm lines and spaces (L/S). After removing the chrome layer, the patterned quartz substrate was coated with the multilayer.

2.2 *Phase Defect Size Measurement Using Scanning Probe Microscope*

All phase defects had their images taken with a combination of SPM (L-Trace II, Hitachi High-Tech Science Corp., Tokyo, Japan) and a triangular pyramid shaped probe (SI-DF40P2, Hitachi High-Tech Science Corp., Tokyo, Japan), as shown in Figs. 2(a) and 2(b), respectively. The typical values of their resonant frequency and spring constant were 300 kHz and 26 N/m. The scan area and speed were set to 600×600 nm^2 and 1.7 Hz, respectively. The numbers of the image pixels were 512 points for the X direction and 256 points for the Y direction.

After capturing an SPM image, the defect size was calculated as illustrated in Fig. 3. Figure 3(a) shows the SPM image (after the image tilt correction) of the multilayer surface that includes the phase defect. Figure 3(b) shows line profiles of the SPM image. The depth of the phase defect was defined as a distance between the surface of the multilayer and the bottom of the phase defect. The width of the phase defect was defined as a full-width at half-maximum (FWHM), as shown in Fig. 3(b). The shaded areas in Fig. 3(b) show the profiles of a pit-type phase defect. The volume of the phase defect was defined as a sum of the shaded areas of all line profiles.

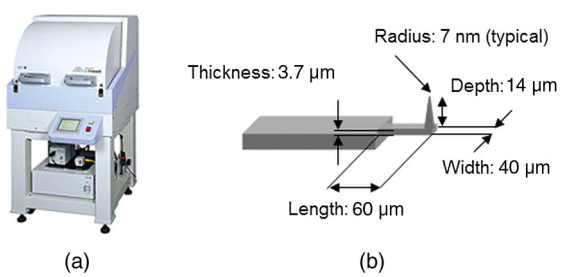

Fig. 2 Phase defect imaging tool and probe: (a) photograph of L-Trace II and (b) schematic model of the cantilever and tip used.

2.3 *Phase Defect Inspection Tool*

To evaluate the relationship for phase defects between size and detection intensity, their images were taken using an actinic blank inspection (ABI) high-volume manufacturing (HVM) model (Lasertec Corporation, Yokohama, Japan). Figure 4 shows a schematic model of the ABI HVM optics. EUV light is focused on the EUV blank. The scattered light due to the existence of the phase defect is collected by Schwarzschild optics with a magnification of 26× and detected by a charge-coupled device camera. The inner and outer numerical apertures (NAs) of the Schwarzschild optics are 0.1 and 0.27, respectively.[23,25]

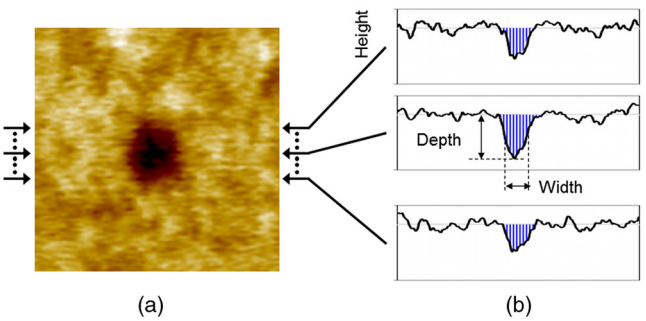

Fig. 3 Calculation methods of the phase defect size and volume: (a) a post-tilt correction SPM image and (b) line profiles of the SPM image along the lines between the arrows indicated in the image (a).

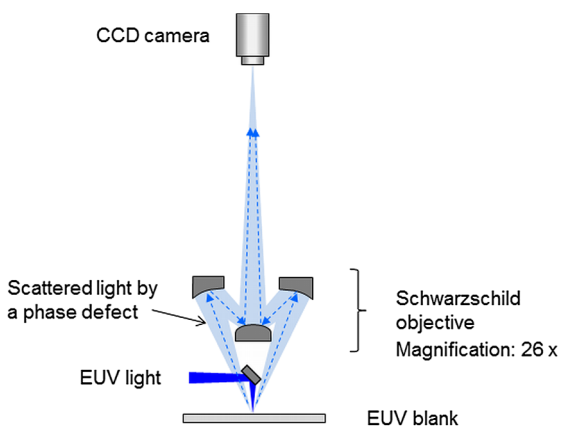

Fig. 4 Schematic model of the optics of the actinic blank inspection tool.

2.4 *Simulation Condition for Defect Printability*

To evaluate the impact of the phase defect on the printed image on wafer, a lithography simulator LAIPH EUV defect printability simulator (KLA-Tencor Corporation, California) was utilized. An NA of 0.33 with a dipole illumination (sigma = 0.4/0.8, pole opening angle = 90 deg) was used to calculate the areal image of 22 nm L/S patterns that corresponded to an 88-nm half pitch on mask. The mask L/S patterns were set in a direction parallel to the projected incoming EUV light. The EUV mask structure was set to be the same as the prepared EUV blank structure with a 66-nm-thick Ta-based absorber layer. The location of the phase defect was defined in terms of its relative distance to the center of a space pattern, as illustrated in Fig. 5(a). A calculated areal image with contour is shown in Fig. 5(b). The critical dimension (CD) was defined as the minimum space width affected by the phase defect. Figure 5(c) shows an example of the calculated result of the printed CD error as a function of phase defect position. In this work, the maximum impacts on the printed CD error were observed from the phase defects located at 0 (zero) nm in position.

3 Results and Discussions

3.1 *Measurement Results of the Programmed Phase Defect Size and Volume*

In this section, the measured size of the programmed phase defect using SPM is described. Each phase defect, as explained in Sec. 2.1, was measured five times for its depth and height. Figure 6(a) shows the measurement result of the phase defect sizes. Each plot indicates an average value of the depth and width of the 10 phase defects. Since the blocks A, B, and C had different etching processing conditions applied, the phase defect sizes became different as was intended, even if the designed lateral sizes were the same. In the same block, the quartz etch depth decreased with decreasing lateral size. This nonlinearity of depth is mainly caused by a proportional relationship between the lateral size of the etch area and the quartz etching speed. At larger lateral sizes of more than $1 \times 1\ \mu m^2$ areas, the etch depths of blocks A, B, and C reached the saturated values of 5.6, 2.9, and 2.1 nm, respectively.

The average volumes of the 10 phase defects are also shown in Fig. 6(b). Apparently, each phase defect shows

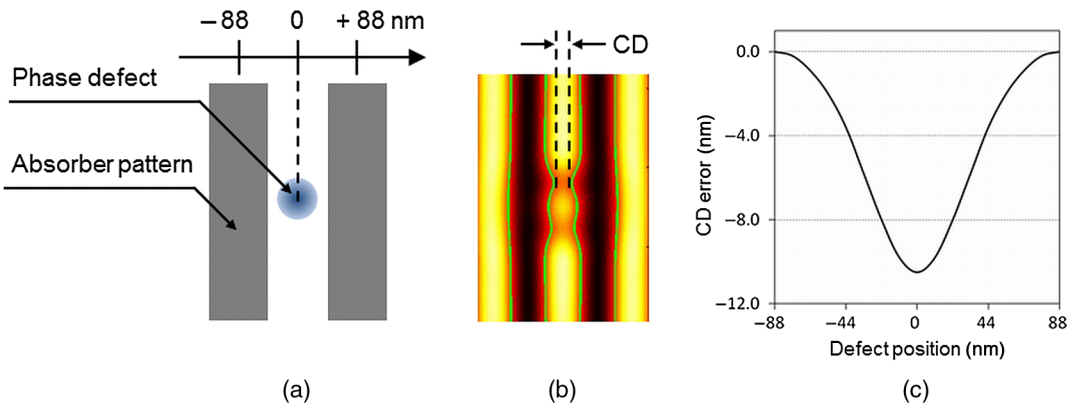

Fig. 5 Calculation method of the CD affected by the phase defect: (a) Top view of a phase defect in the 88 nm L/S pattern. The scale indicates the phase defect position relative to the center of the space pattern. (b) Calculated areal image and contour. (c) Calculated CD error as a function of the phase defect position. The target space CD on the wafer is 22 nm.

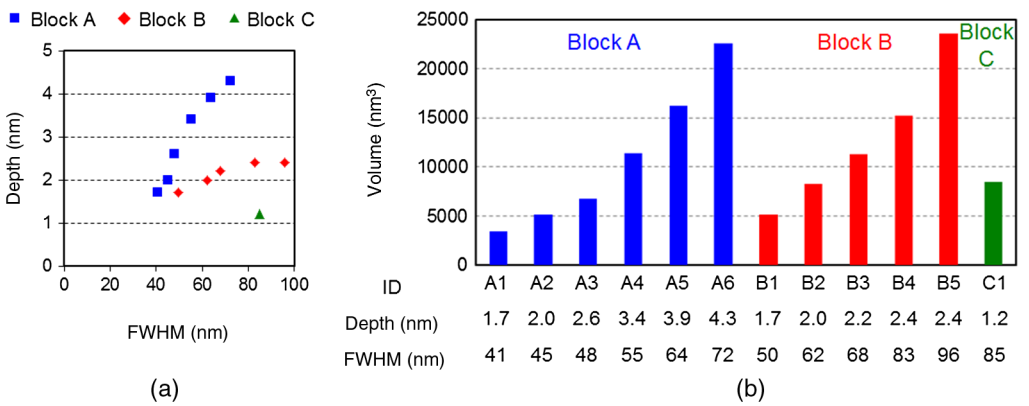

Fig. 6 Summary of the obtained sizes for the programmed phase defects: (a) depth and width. (b) volume, together with average depth and width.

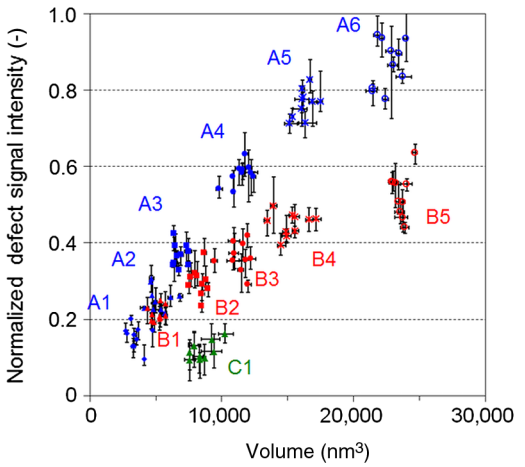

Fig. 7 Normalized defect signal intensities as a function of the phase defect volume. IDs from A1 to C1 correspond to the same IDs in Fig. 6(b).

different volumes within the same block. However, there are some combinations of phase defects, such as IDs A2 and B1 or IDs A4 and B3, that have different depths and widths even when their volumes happen to be almost the same. These combinations are useful in analyzing the impact of the defect size or volume on defect detection signal intensity.

3.2 *Defect Detection Signal Intensity*

The influence of the phase defect volume on the ABI HVM defect signal intensity (DSI) was evaluated. The image of each phase defect was acquired five times with an exposure time of 40.5 ms, and the DSIs were calculated from those images. Figure 7 shows the normalized DSI as a function of the phase defect volume obtained by SPM (see Fig. 3). As shown in Fig. 1, there are 10 phase defects for each design size. Plots represent the average value of the phase defect volume and DSI. Due to the measurement repeatability of the phase defect volume and DSI, all the plots show error bars along the horizontal and vertical axes, respectively. As shown in Fig. 6(b), there are some combinations of phase defect IDs with almost the same volume but different depths and widths. Comparing between A6 and B5, A4 and B3, B2 and C1, each combination had almost the same phase defect volume but a different DSI. From a view point of the defect shape, the higher DSI case, specifically, A6, A4, and B2, shared a common trend of deeper phase defects than their respective counterparts. This tendency was also observed at the small-size combination of A2 and B1, where the volumes were almost the same; the volume of A2 was 1.01 times larger than that of B1, but the average DSI value of A2 was 1.2 times larger than that of B1. Although the ABI HVM can detect the phase defect on the EUV blank, these results indicated that the volume of the phase defect is hard to predict with only the information of its DSI.

3.3 *Influence of the Phase Defect on Wafer Printability*

Although there is a trend-like relationship between the phase defect volume and the DSI, the important point is to know which measured value can be seen as reliable to predict the impact of the phase defect on a wafer printed CD. To calculate the wafer printed CD impact for various shapes or volumes of phase defects, a lithographic simulator was employed. Figure 8 shows the calculated results of the printed CD errors as a function of the phase defect positions. The depths and FWHMs of the phase defects, shown in Fig. 6(a), were used to calculate the printed images. The phase defects of A4 and B3 had almost the same volumes of 11450 and 11329 nm^3, respectively. However, the influences of the phase defects on the printed CDs were quite different. A4 caused more than 12 nm of CD error even though B3 caused only 8 nm of CD error. The same tendency was observed in other combinations of B2 and C1, and of A2 and B1, as shown in Figs. 8(b) and 8(c), respectively. These results indicate that the wafer printability cannot be predicted only from the information of the phase defect volume.

Figures 9(a) and 9(b) represent the CD error to print 22 nm L/S on wafer as functions of the phase defect volume and width, respectively. A4, A5, and A6 are not shown because these phase defects caused lines bridging defects on the wafer, as shown in Fig. 8(a). Judging the influence of different size phase defects in the same block on a printed CD, the larger phase defects caused greater CD errors. However, compared with phase defects between groups A,

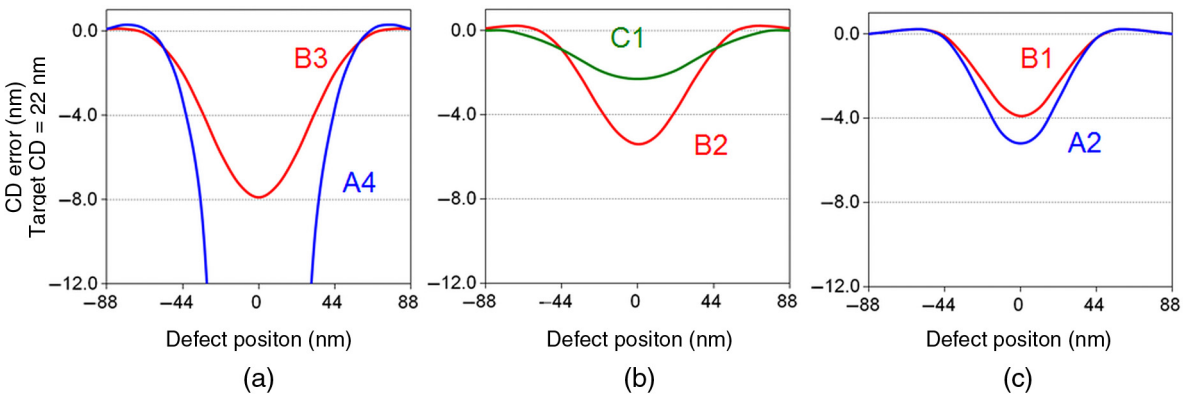

Fig. 8 Calculated CD errors as a function of the phase defect position. Comparison with: (a) A4 (volume is 11450 nm^3) and B3 (11329 nm^3), (b) B2 (8328 nm^3) and C1 (8518 nm^3), (c) A2 (5209 nm^3) and B1 (5145 nm^3).

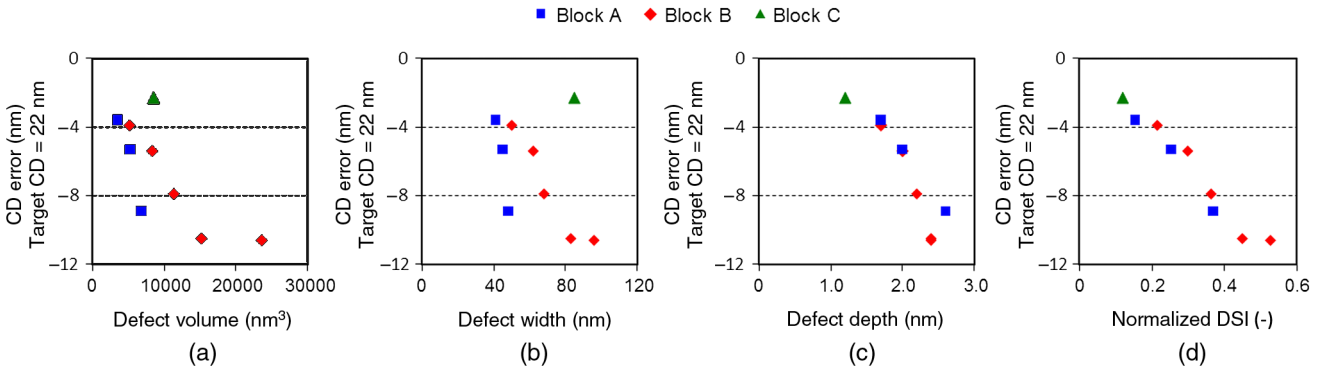

Fig. 9 Influences of the phase defect on the printed space CD on a wafer as functions of (a) phase defect volume, (b) phase defect width, (c) phase defect depth, and (d) detection signal intensity.

B, and C, there are relatively weak correlations between the phase defect size and CD error. For example, among the phase defects in blocks A and C, the phase defect in block C was the largest in volume and width but had the least influence on the wafer printed CD. On the other hand, as shown in Figs. 9(c) and 9(d), the CD errors caused by the phase defects in blocks A, B, and C were almost linear with respect to the defect depths and DSIs. Linear regression analysis showed strong correlations between the defect depth and CD error, and DSI and CD error. The coefficient of correlation values were 0.89 and 0.97, respectively, whereas the correlation factors between the phase defect volume and CD error, and the defect width and CD error were only 0.75 and 0.44, respectively. Such a strong correlation, especially between the DSI and CD error, allowed distinguishing the lithographic impacts caused by the phase defects A2 and B1 that had DSIs of 0.21 and 0.25, respectively, although the difference in the volume was negligibly small. These phase defects caused CD errors of −3.9 and −5.3 nm, respectively. As a result, the printed CD error had a strong correlation with DSI and defect depth rather than the phase defect volume and width.

4 Summary and Conclusion

In order to predict the printing impact on a wafer for phase defects embedded in the multilayer mirror of an EUVL mask, two types of phase defect measurement methods were applied to characterize the phase defects and calculate their impact on the printed CD on a wafer. A programmed phase defect mask was fabricated that comprised pit-type phase defects of different depths in the range of 30, 40, 50, 60, 70, 80, and 100 nm in diameter. The volumes of the phase defects were measured with SPM, and their DSIs were calculated from the images acquired by ABI HVM. It was found that the DSIs did not correlate directly with the phase defect volumes. Next, the influence of the phase defects on a wafer printed image of 22 nm L/S patterns was calculated using a lithography simulator. The calculated results indicated that the printed CD error had a strong correlation with DSI and defect depth rather than with phase defect volume and width. The correlation factors were 0.97, 0.89, 0.75, and 0.44, respectively. As a result, the influence of a phase defect on a printed CD error can be predicted from the value of its DSI.

Acknowledgments

The authors are grateful to Hiroki Miyai and Tomohisa Ino of Lasertec Corporation for their technical advice and inspection using ABI HVM and also to Noriaki Takagi of EIDEC for his technical advice and fruitful discussion. This work was supported by New Energy and Industrial Technology Development Organization (NEDO) and Ministry of Economy, Trade and Industry (METI).

References

1. U. Dietze et al., "Effective EUVL mask cleaning technology solutions for mask manufacturing and in-fab mask maintenance," *Proc. SPIE* **7985**, 79850N (2011).
2. N. Takagi et al., "Evaluation of the contamination removal capability and multilayer degradation in various cleaning methods," *Proc. SPIE* **7823**, 782327 (2010).
3. T. Shoki et al., "Improvement of total quality on EUV mask blanks toward volume production," *Proc. SPIE* **7636**, 76360U (2010).
4. H. Kinoshita et al., "Mask technology of extreme-ultraviolet lithography," *Proc. SPIE* **3412**, 358–368 (1998).
5. Y. Arisawa et al., "Impact of EUV mask roughness on lithography performance," *Proc. SPIE* **8679**, 86792S (2013).
6. Y. Tanaka et al., "Fabrication of 35 nm via-hole patterns for interconnect test chips with EUV lithography," *Proc. SPIE* **7636**, 76362D (2010).
7. N. Sugie et al., "Resist outgassing characterization based on the resist compositions and process," *Proc. SPIE* **8679**, 86792E (2013).
8. M. Naka et al., "Capability of model EBEYE M for EUV mask production," *Proc. SPIE* **8522**, 85220K (2012).
9. T. Kamo et al., "Evaluation of EUV mask defect using blank inspection, patterned mask inspection, and wafer inspection," *Proc. SPIE* **7969**, 79690J (2011).
10. R. Hirano et al., "Evaluation of novel projection electron microscopy (PEM) optics for EUV mask inspection," *Proc. SPIE* **8679**, 86791T (2013).
11. S. Mangan et al., "Results from a novel EUV mask inspection by 193 nm DUV system," *Proc. SPIE* **7638**, 76383S (2010).
12. F. Aramaki et al., "Development of new FIB technology for EUVL mask repair," *Proc. SPIE* **7969**, 79691C (2011).
13. S. Kanamitsu et al., "Prospect of EUV mask repair technology using e-beam tool," *Proc. SPIE* **7823**, 782322 (2010).
14. T. Amano et al., "Study of EUV mask defect repair using FIB method," *Proc. SPIE* **7823**, 782323 (2010).
15. Z. Zhang et al., "Investigation of resist effects on EUV mask defect printability," *Proc. SPIE* **6730**, 673016 (2007).
16. T. Liang et al., "EUV mask pattern defect printability," *Proc. SPIE* **6283**, 62830K (2006).
17. H. Aoyama et al., "Repair specification study for half-pitch 32-nm patterns for EUVL," *Proc. SPIE* **6730**, 67305L (2007).
18. D. V. Heuvel et al., "Natural EUV mask blank defects: evidence, timely detection, analysis and outlook," *Proc. SPIE* **7823**, 78231T (2010).
19. T. Murachi et al., "Fiducial mark requirements from the viewpoints of actinic blank inspection tool for phase-defect mitigation on EUVL mask," *Proc. SPIE* **8522**, 85221U (2012).
20. T. Murachi et al., "Phase defect mitigation strategy: fiducial mark requirements on extreme ultraviolet lithography mask," *Proc. SPIE* **8322**, 83221Q (2012).

21. T. Murachi et al., "Registration accuracy improvement of fiducial mark on EUVL mask with MIRAI EUV ABI prototype," *Proc. SPIE* **8679**, 86791U (2013).
22. R. Jonckheere et al., "Repair of natural EUV reticle defects," *Proc. SPIE* **8166**, 81661G (2011).
23. A. Tchikoulaeva et al., "EUV actinic blank inspection: from prototype to production," *Proc. SPIE* **8679**, 86790I (2013).
24. T. Amano et al., "Phase defect detection signal analysis: dependence of defect size variation," *J. Micro/Nanolith. MEMS MOEMS* **14**(1), 013502 (2015).
25. T. Yamane et al., "Phase defect analysis with actinic full-field EUVL mask blank inspection," *Proc. SPIE* **8166**, 81660G (2011).
26. H. Miyai et al., "The capability of high magnification review function for EUV actinic blank inspection tool," *Proc. SPIE* **8701**, 870118 (2013).
27. T. Amano et al., "Impact of the phase defect structure on an actinic dark-field blank inspection signal and wafer printability," *Proc. SPIE* **8322**, 832234 (2012).
28. N. Takagi et al., "Effect of phase defect shape on ABI signal intensity and defect image intensity on wafer with simulation," *Proc. SPIE* **8679**, 86791X (2013).
29. T. Suzuki et al., "Defect analysis on actinic blank inspection tool," *Proc. SPIE* **9256**, 92560O (2014).
30. T. Terasawa et al., "Actinic phase defect detection and printability analysis for patterned EUVL mask," *Proc. SPIE* **7636**, 763602 (2010).

Tsuyoshi Amano received his BS and MS degrees in applied chemistry from Keio University in 1997 and 1999, respectively. He joined Dai Nippon Printing Co. Ltd., where he carried out research on mask process, metrology, and repair technology. In 2011, he was assigned to EIDEC, and since then he has been engaged in the development of patterned masks and blank inspection tools.

Tsukasa Abe: Biography is not available.